Nano Research

ISSN 1998-0124 CN 11-5974/O4
https://doi.org/10.26599/NR.2026.94908758

Decoding lithium plating evolution at ultralow temperatures through real-time FBG strain monitoring

Fan Zhang[1], Di Lu[1](✉), Peitao Xiao[1], Xianxian Shi[1], Shu Hong[2], Yufang Chen[1](✉)
[1] College of Aerospace Science and Engineering, National University of Defense Technology, Changsha 410000, China
[2] Tianjin Lishen Battery Joint Stock Company Limited, No.6, Lanyuan Road, Huayuan Industrial Park, Tianjinn 300384, China

Nano Res., **Just Accepted Manuscript** • https://doi.org/10.26599/NR.2026.94908758
https://www.sciopen.com/journal/1998-0124 on Apr. 20, 2026

© The Authors(s)

Just Accepted

This is a "Just Accepted" manuscript, which has been examined by the peer-review process and has been accepted for publication. A "Just Accepted" manuscript is published online shortly after its acceptance,which is prior to technical editing and formatting and author proofing. Tsinghua University Press (TUP) provides "Just Accepted" as an optional and free service which allows authors to make their results available to the research community as soon as possible after acceptance. After a manuscript has been technically edited and formatted, and the page proofs have been corrected, it will be removed from the "Just Accepted" web site and published officially with volume and article number (e.g., *Nano Research*, **2025**, *18*, 94906990). Please note that technical editing may introduce minor changes to the manuscript text and/or graphics which may affect the content, and all legal disclaimers that apply to the journal pertain. In no event shall TUP be held responsible for errors or consequences arising from the use of any information contained in these "Just Accepted" manuscripts. To cite this anuscript please use its Digital Object Identifier (DOI®),which is identical for all formats of publication.

Just Accepted

Template for Preparation of Manuscripts for *Nano Research*

TABLE OF CONTENTS (TOC)

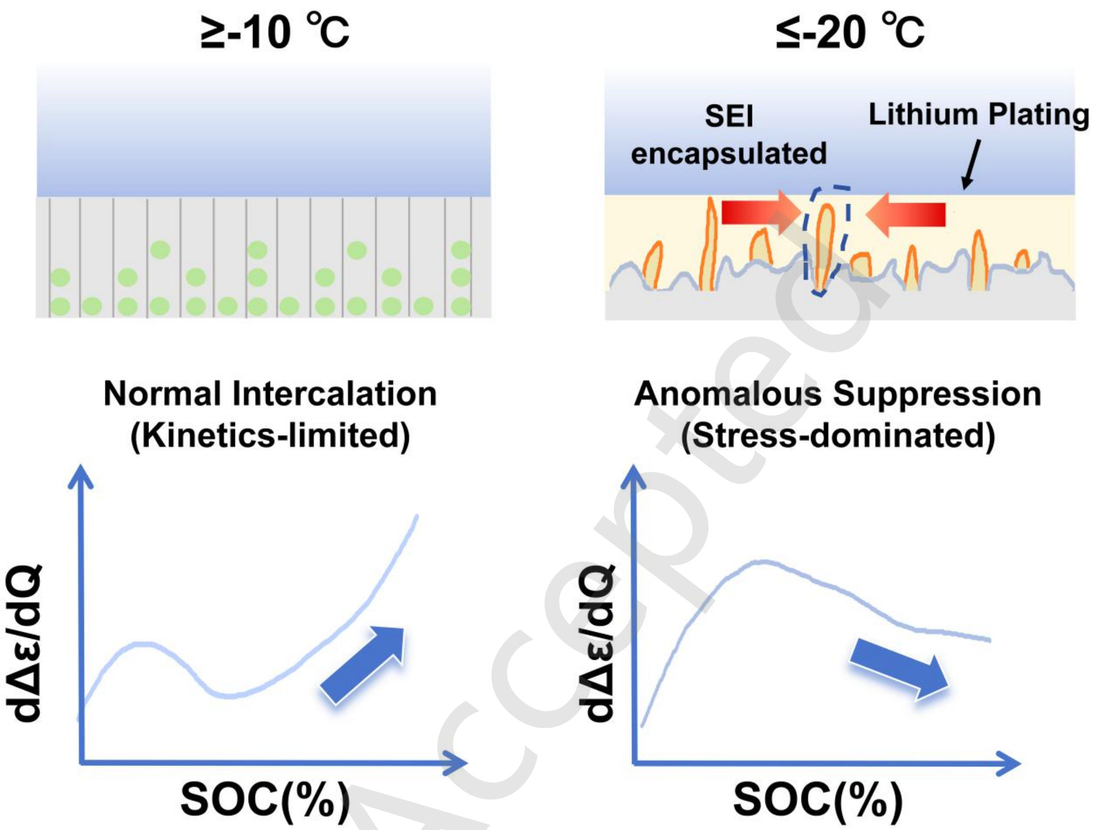

Embedded fiber sensing reveals a fundamental shift in lithium plating mechanisms at cryogenic temperatures. Real-time strain signatures decode how the process transitions from normal intercalation to an anomalous, stress-dominated state governed by internal mechanical constraints.

Nano Research

Open Access

Review Article/Research Article Please choose on

Decoding lithium plating evolution at ultralow temperatures through real-time FBG strain monitoring

Fan Zhang[1], Di Lu[1], Peitao Xiao[1], Xianxian Shi[1], Shu Hong[2], and Yufang Chen[1].

[1]*College of Aerospace Science and Engineering, National University of Defense Technology, Changsha 410000, China*
[2]*Tianjin Lishen Battery Joint Stock Company Limited, No.6, Lanyuan Road, Huayuan Industrial Park, Tianjinn 300384, China*

Received: 18 February 2026; **Revised:** 1 April 2026; **Accepted:** 20 April 2026

Address correspondence to Di Lu, ludi@nudt.edu.cn; Yufang Chen, chenyufang@nudt.edu.cn

Cite this article: *Nano Research*, 2026, 19, 94908758 https://doi.org/10.26599/NR.2026.94908758

ABSTRACT: Real-time detection of lithium plating under extreme conditions is critical for battery safety. Here, we use embedded fiber Bragg grating (FBG) sensors to achieve real-time monitoring of mechanical strain evolution in operating graphite pouch cells. At ultralow temperatures (–20 and –30 °C), we observe an anomalous suppression in differential strain ($d\varepsilon/dQ$) during late-stage charging . Specifically, the strain generation rate is severely constrained, dropping to approximately 0.1 με/mAh at high state-of-charge (SOC)—a stark contrast to the normal intercalation baseline of ~0.3 με/mAh observed under milder, non-plating conditions. Through synchronized electrochemical analysis and post-mortem characterization, we show that this mechanical anomaly reflects a fundamental shift in plating behavior: at cryogenic temperatures, internal mechanical constraints imposed by prior plating and SEI densification suppress further expansion, altering the progression of lithium deposition. The real-time strain signals also reveal a dynamic competition between SEI fracture-repair cycles and lithium re-plating, providing insight into coupled degradation mechanisms governing battery failure. This work establishes an *in-situ* diagnostic tool for battery failure and offers new mechanistic understanding of lithium plating under extreme conditions.

KEYWORDS: Li plating, strain monitoring, fiber Bragg grating (FBG) sensor, battery degradation

1 Introduction

Electrical vehicles are gaining their popularity over recent years for governments and public are working together to decrease the emission of CO_2 to reach the goal of Carbon Neutrality Vision and the of 2030^+roadmap[1,2].However, fast charging for battery in EV has the problem of the plating of Li metal and charging at low temperature[3] can also lead to Li-plating which will sacrifice battery safety[4] for it would trigger the growth of Lithium dendrites. Charging at high state of charge (SOC) can also lead to high possibility of Li-plating [4]. From a structural perspective, factors such as a low N/P ratio, unoptimized anode overhang regions, intrinsic electrode defects [5], and poor electrolyte wettability [6] can induce severe cell imbalance, thereby exacerbating the risk of localized lithium plating. So, there is an urgent need to take a detailed look at the principle of Li-plating and take practical measures to restrain it for battery safety and long life.

Under the situation mentioned above, the lithium-ion influx exceeds the anode's intercalation capability, battery polarization increases significantly and the anode potential drops below 0 V versus Li^+/Li(or $\Delta\eta > \eta_{Gr}-\eta_{Li}$)[7,8], so lithium deposition occurs on the anode surface as shown in Fig. 1(a). As the reaction proceeds, part of the plated lithium layer reacts with the electrolyte and solid electrolyte interphase (SEI) forming a thick, fragile SEI, which easily fractures, permanently isolating the lithium fragments. This process irreversibly consumes active lithium and electrolyte, contributing directly to the formation of "dead lithium" and rapid capacity fade. In some occasion, the initially formed lithium layer is uneven. Microscopic defects and uneven current distribution create hotspots with higher local current density. Some portion, due to the instability of the SEI structure, becomes detached from the electrode in discharging process, accelerates "dead lithium" formation. It is worth mentioning that lithium plating and graphite intercalation are competing reactions. The relative rates of these two processes determine the safety and health of the battery. The occurrence of lithium plating leads to lithium loss and increased instability of the SEI layer. In severe cases, lithium dendrites penetrate the separator, leading to an internal short circuit, compromising battery safety [8–10].

In previous studies, researchers have employed electrochemical techniques and physical detection methods to identify lithium plating [11–14]. Electrochemical techniques primarily rely on differences in the electrochemical behavior between lithium intercalation into graphite and lithium plating. These methods typically involve differential voltage (DV)[15] and incremental capacity (IC) [16] analysis of the battery. The peaks in the DV curve represent phase transition processes [17–19]. Notably, recent investigations have identified the inflection point on the differential voltage curve during the discharging process as a precise criterion for the onset of lithium plating, offering a theoretical benchmark for triggering detection [20]. During discharge, the reduction reaction of lithium on the anode surface occurs prior to the reduction of lithium intercalation compounds in the graphite. Under a low-current discharge or relaxation process, a small trough in the differential voltage (DV) curve appeared. The lowest point of this trough indicates the complete conclusion of the reduction of reversible lithium [21]. Each peak in the incremental capacity (IC) curve corresponds to an electrochemical reaction, with the peaks indicating phase equilibria. For instance, Adam et al. [22] utilized peaks appearing in the IC curve during the charging process to identify the lithium plating process. And in-situ detection of reversible lithium plating can be achieved by monitoring the open-circuit voltage relaxation profile after charging. A distinct voltage plateau—or double-plateau feature—indicates that plated lithium remains electrically connected and is undergoing stripping, whereas its absence suggests irreversible "dead lithium" formation [23]. Physical analysis methods generally involve destructive analysis of the battery or employ specially designed in-situ cells for physical detection, which are not conducive to the non-destructive identification of lithium plating under operating conditions. Several research studies have highlighted the critical trade-offs between sensitivity and practical operando implementation for detection of lithium plating [24].

In recent years, a growing number of studies have emerged that utilize thickness or pressure monitoring techniques for lithium plating detection. Gao et al. [25] proposes a new real-time lithium plating detection method based on characteristic peaks in the expansion force–voltage differential curve, which does not require extra rest or constant-voltage data and is more accurate than traditional detection methods. Huang et al. [26] employed an external pressure measurement setup and observed that the pressure measured during high-rate charging exceeds the threshold recorded under low-rate conditions, thus indicating the onset of plating. Yang 's group has conducted systematic research into the mechanism and monitoring of lithium deposition, revealing the three-stage lithium deposition under fast charging and its coupling mechanism with SEI and electrolyte decomposition[27]; they further clarified that heterogeneous lithiation is a key driver of lithium plating and proposed a cooperative suppression strategy combining interface regulation and particle homogenization[28]; moreover, they developed an in situ impedance-thickness coupling technique to enable multidimensional dynamic monitoring of the lithium evolution process[29].Yan et al.[30] detected lithium plating by monitoring the pressure differential plateau. Most recently, Chen et al. [31] proposed an operando detection method by decoupling the macroscopic expansion force signal, introducing indicators to quantify both reversible and irreversible lithium deposition. Furthermore, the electrochemo-mechanical coupling has been further explored to unlock the hidden dynamics of lithium plating under stacking pressure, revealing how external stress fundamentally modulates the plating/stripping kinetics [32]. Although these studies have successfully correlated macroscopic mechanical signals with plating behavior using external sensors, most existing mechanical monitoring techniques—such as overall thickness or swelling force measurements(e.g., dilatometers or external load cells)—remain limited to spatially averaged, cell-level responses. Because these sensors are placed outside the battery, the measured macroscopic expansion signals often suffer from temporal delay and mechanical buffering caused by the cell casing (e.g., the aluminum-plastic film in pouch cells).Under realistic cell packaging and operating conditions, these methods generally cannot precisely and operando locate the micro-scale initiation sites of lithium plating inside the electrode stack, nor can they track the full dynamic evolution from early nucleation onward. The subtle mechanical signature of early-stage plating is easily masked by background strains such as graphite intercalation. More critically, current external techniques still lack the capability to directly reveal the intrinsic chemo-mechanical coupling that governs the plating process under extreme conditions at the micro- to nano-scale. Therefore, the development of novel monitoring approaches with high spatial resolution, capable of capturing local mechanical evolution in situ without casing interference, is essential for fundamentally understanding the mechanism of lithium plating and achieving early warning.

To overcome these limitations, we introduce an embedded optical fiber sensing strategy based on fiber Bragg grating (FBG) sensors [33]. Unlike external macroscopic sensors, bare FBG sensors can be integrated directly inside the cell at the electrode/separator interface. This internal configuration fundamentally circumvents the buffering effect of the cell packaging, offering high-resolution, zero-delay monitoring of local interfacial micro-strain variations. This work establishes a mechanical monitoring framework that captures real-time, spatially resolved strain evolution during lithium plating. By directly correlating these strain fingerprints with electrochemical processes and postmortem analysis, we elucidate the transition from kinetics-limited behavior to stress-dominated degradation pathways. Distinct mechanical signatures are observed during reversible intercalation, plating onset, and dead lithium accumulation, with anomalous strain responses (e.g., a late-stage decrease in differential strain) signaling shifts in the underlying mechanism. Additionally, dynamic SEI repair evolution concurrent with lithium plating is identified. These findings provide a mechanical perspective to understand lithium plating evolution and its role in battery failure.

2 Results and discussion

2.1 FBG Validation and Stage-wise Fingerprints

Given that the deintercalation and intercalation of lithium ions in electrode materials are key processes for energy conversion, it is essential to focus on the evolution of stress/strain within batteries, as the reversibility of electrode materials can be well characterized by strain. For anode materials with a graphite intercalation mechanism, changes in lattice parameters occur repeatedly during the charging and discharging processes, leading the electrode material to undergo repeated lattice expansion or contraction. During the process of intercalation of lithium, different lithium stages are formed (including the stages 1L, 4L, 3L, 2L, 2, and1[34]). When graphite is fully lithiated to

LiC_6, the total volume change rate reaches approximately 13% [7,35]. For NCM cathode, the volume change is 3% (1% in thickness), but in this experiment we assume the volume expansion of the cathode electrode to be consistent each time, and only consider the portion of the overall volume change involving the anode electrode, making the method of strain monitoring for lithium deposition closer to the actual situation.

This study employed embedded Fiber Bragg Grating (FBG) sensors to monitor the strain of the battery in real time. The sensor is sealed in the battery before inject electrolyte, with the sensor point positioned at the center of the battery. The working principle is that the volume change of the battery during cycling causes axial strain in the optical fiber, thereby altering the period of the internal grating, which in turn leads to a shift in the central wavelength of the reflected light. As shown in Fig. 1(b), when no lithium deposition occurs in the battery, the degree of expansion during graphite charging is the same as the degree of contraction during discharging. And the asymmetric strain evolution observed in the full-cell configuration can be attributed to the formation of "dead lithium". During charging, lithium plating occurs, leading to an irreversible volume expansion. Crucially, during subsequent discharging, a portion of this plated lithium loses electrical contact with the anode (e.g., due to dendrite fracture or thick SEI encapsulation) and becomes electrochemically inactive "dead lithium". This "dead lithium" fails to contribute to the contraction during discharge, resulting in the net residual strain and the broken strain symmetry captured by the FBG sensor. This provides direct mechanical evidence linking the irreversible plating morphology to capacity loss in practical full cells. As the cycle progresses, this asymmetry continues to intensify, indicating the continuous accumulation of "dead lithium", which ultimately leads to a sharp deterioration in battery performance. By tracking the movement of this wavelength in real time, the information on the strain evolution of the battery can be quantitatively obtained. As illustrated in Fig. 1(b), the FBG signal reveals a clear evolution with cycling. Initially, during healthy intercalation/de-intercalation, the response is characterized by a symmetric, closed hysteresis loop with zero net residual strain after a full cycle, indicating reversible behavior. As cycling progresses, the onset of lithium plating introduces an irreversible strain component, which manifests as a continuous, monotonic increase in the baseline wavelength shift ($\Delta\lambda$) while the reversible loop amplitude remains largely intact. Ultimately, extensive plating leads to dendrite fracture and the formation of electrochemically inactive “dead lithium,” resulting in a fundamentally altered FBG signature: both the strain amplitude and battery capacity degrade significantly.

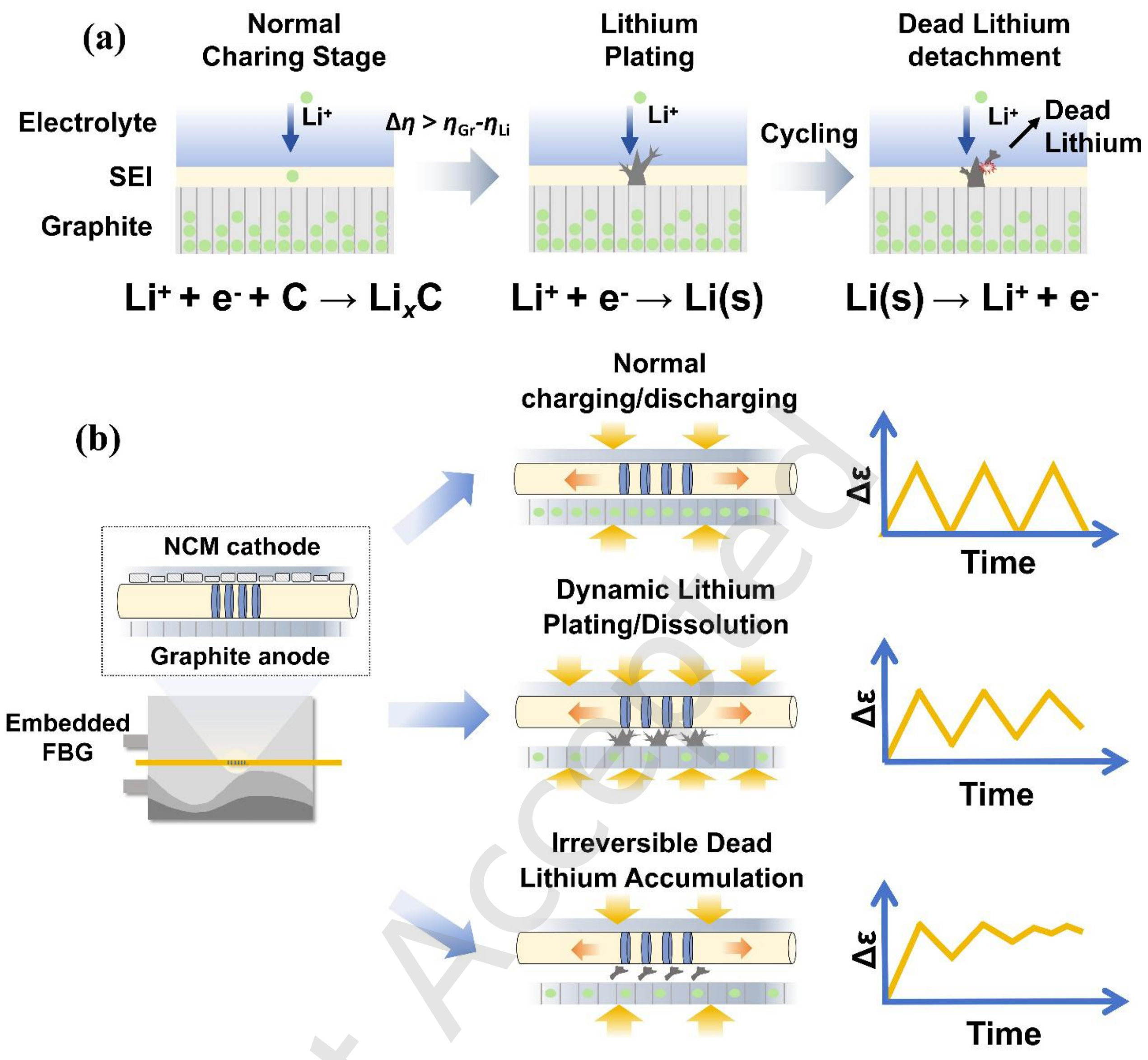

Figure 1Evolution Mechanism of Lithium Plating and Principle of Operando Dynamic Monitoring via Embedded Fiber Bragg Grating. (a) Schemes of Lithium Plating and "dead lithium" Formation (b) Principle of Dynamic Lithium Plating Detection Using FBG.

Firstly, we conducted 0.1C CC charging/discharging test at 45 °C. The strain variation in Fig. 2(a) shows that its strain signal was consistent with the changes in the interlayer spacing of graphite lithium compounds at each stage. The interlayer spacing shows linear variation from the initial state to the 2L stage (LiC_{18}), remains relatively constant during the transition from 2L to the 1L stage (LiC_{12}), and increases further in the final fully lithiated stage [30]. This indicates that this method has a certain degree of reliability. Figure 2(b) is a diagram of the experimental setup. Before the test begin, we applied constant pressure to the battery and allowed it to rest for a period of time to ensure that each battery has the same stress state before the test begin. Figure S1 in the ESM presents the strain and differential strain signal during constant current charge-discharge tests on the battery at -10 °C, and 10 °C, ranging from 0.1C to 0.5C. A comprehensive analysis of the electrochemical signatures revealed a pronounced dual dependence of the system's behavior on both operational temperature and applied current rate. We can see that as the charging rate increases or the temperature decreases, the differential strain changes more mildly. Significant disparities were observed not only between the strain profiles and corresponding differential capacity (dQ/dV) curves obtained at identical temperatures under varying C-rates but also between those recorded at a fixed C-rate across different temperatures. These marked differences in the dQ/dV peaks, including their position, intensity, and shape, unequivocally indicate that kinetic and thermodynamic limitations are interdependently governed by thermal conditions and charge/discharge dynamics, leading to fundamentally altered phase transition pathways and reaction homogeneity. Unlike the results of Huang et al. [26], the peak values of strain differential signals obtained from charging and discharging at different rates at the same temperature do not lie on a straight line. It is reasonably speculated that this is due to the significant impact of high-rate charging on capacity at low temperatures.

We first analyze the results obtained at -10 ℃, and characterize the battery graphite electrode charged to 4.2 V at this temperature. From Fig. 2(d), it can be observed that the strain variation decreases as the rate increases during the charging process different from the normal graphite lithiation process strain variation, which shows that the differential strain curves in the high SOC region exhibit a decreasing trend as the C-rate increases. A demarcation is observed at 0.3C. It can be seen that the curves for the first two lower rates show an increase, whereas the curves for the subsequent higher rates decrease. Corresponding differential capacity curves in Fig. a(c) during discharge show lithium stripping plateaus only for the latter three higher C-rates. This confirms that lithium plating occurred during charging at 0.3C, 0.4C, and 0.5C. While in contrast at 10 ℃ in Fig. 2(g), in the later stage of charging, the strain differential curves show an upward trend, with no irreversible lithium stripping peak in dV/dQ curve [36]. Figure S2 in the ESM is the Raman tests, which confirm the presence of lithium on the electrode surface at 0.3C. These proves the effectiveness of using strain differential curves to determine lithium deposition.

This set of characterizations (XRD, SEM) consistently demonstrates that increasing the charging rate under low-temperature conditions not only triggers lithium plating but fundamentally alters its failure pathway through intensified kinetic competition. XRD patterns shown in Fig. S4 in the ESM reveal that higher rates (0.3C–0.5C) induce significant broadening of the $\mathrm{LiC_{12}/LiC_{18}}$ (002) peak, indicating severe structural heterogeneity and non-uniform lithiation—a direct precursor to plating. As shown in Fig. 2(i), the surface morphology exhibits a clear dependence on the C- rate. While no evidence of plating is detected at 0.1C, dendritic lithium becomes discernible at 0.3C, and at 0.5C, the surface is largely covered by spherical, SEI- encapsulated features. This morphological shift points to a rate- dependent competition between plating and passivation: the high overpotential at 0.5C triggers rapid and extensive nucleation of lithium, while the rapidly expanding interface promotes SEI formation that encapsulates the nascent nuclei, forming spherical “dead Lithium” rather than extended dendrites. This encapsulation- limited growth is consistent with the slowed strain increase observed at 0.5C.

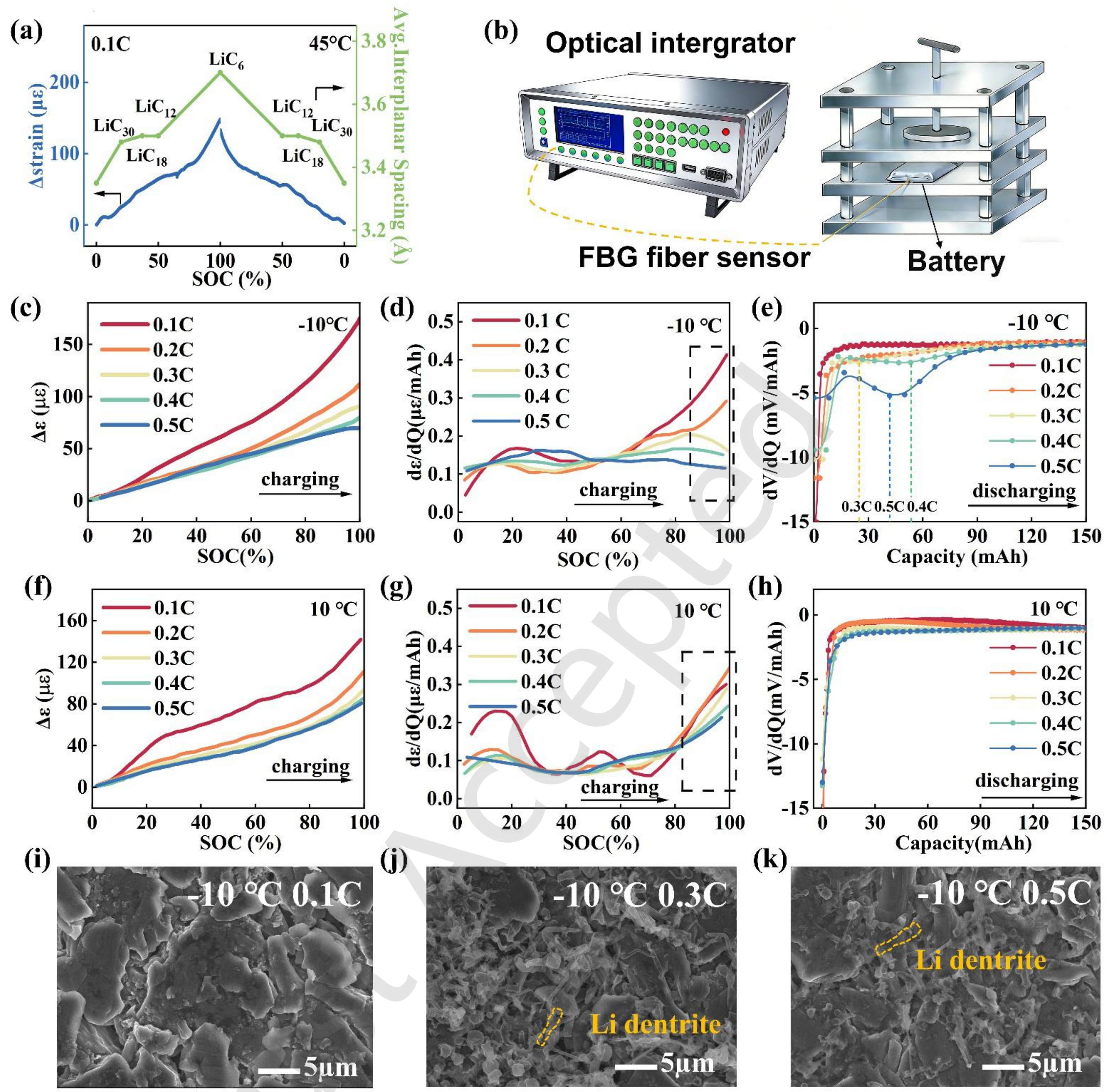

Figure 2 (a) Diagram of signal of 45 °C 811||Gr battery under 0.1C CC charge and discharge and graphite lithiation layer spacing changes (b) Schematic diagram of experimental setup (c-e) Strain variation, strain differential curve diagram (dε/dQ) for charging and dV/dQ for discharging at -10 °C (f-h) Strain variation, strain differential curve diagram(dε/dQ) for charging and dV/dQ for discharging at 10 °C (i-k) SEM images of the anode electrodes charged at 0.1C,0.3C and 0.5C at -10 °C.

2.2 Discovery of a Stress Dominated Plating Regime at Cryogenic Temperatures

In order to systematically study the lithium plating behavior of batteries at different temperatures, we conducted strain monitoring on batteries from 10 °C to -30 °C. Figure 3(a-d) reveals the lithium plating behavior. It can be seen that as the temperature decreases, the strain differential variation tends to flatten. Especially below -20 °C, the characteristic curve of graphite lithium insertion stage no longer appears, and the differential strain curve shows a gradually decreasing trend with the increase of SOC. To quantitatively evaluate this electro-chemo-mechanical confinement, the differential strain (dε/dQ) was meticulously analyzed. Under milder, non-plating conditions (e.g., 0 °C and 10 °C), the battery typically exhibits a baseline terminal strain generation rate of approximately 0.3 με/mAh. Even at −10 °C, the strain rate surges to ~0.4 με/mAh at the end of charging due to unconstrained expansion (Fig. 3c). In stark contrast, taking −30 °C as a quantitative example, the overall strain rate is heavily constrained from the very beginning, peaking at only ~0.18 με/mAh. As charging progresses into the late stage (>90% SOC), the dε/dQ curve exhibits a continuous and significant decay, eventually dropping to roughly 0.1

με/mAh. As charging progresses into the late stage (>90% SOC), the dε/dQ curve exhibits a continuous and significant decay, eventually dropping to roughly 0.09 με/mAh. This ~50% internal quantitative decline provides a robust mathematical indicator of severe spatial confinement.

This transformation in mechanical behavior is corroborated by multi-scale characterization. The dQ/dV curve in Fig. 3(e) displays prominent, sharp peaks, which means that after reaching the critical potential, the charge transfer process suddenly switches from mainly intercalation reactions to mainly metal deposition reactions. A large amount of capacity is generated through lithium plating reaction within a narrow voltage window and may also indicate the occurrence of uneven lithium deposition. Crucially, ex-situ XRD provides direct structural evidence pointing to a macroscopic stress build-up in Figure. 4(a). The characteristic $\mathrm{LiC_{12}/LiC_{18}}$ (002) peak exhibits a non-monotonic, temperature-dependent shift. The peak first shifts to a higher angle from 10 °C to –20 °C, indicating a lower degree of lithiation due to kinetic hindrance, but then shifts to a lower angle at –30 °C. This anomalous low-angle shift contradicts the expected trend of reduced lithiation at lower temperatures. This suggests that heterogeneous lithiation induces lattice strain in the graphite. This structural signature is consistent with, and provides direct evidence for, a transition to a stress-influenced or stress-dominated process. Post-mortem SEM in Fig. 4(b) accompanied with Fig.S5 confirms the severity of plating at cryogenic temperatures, showing exacerbated graphite fragmentation and clear lithium dendritic structures which is consistent with the lithium stripping peak reflected in the dV/dQ curve in Fig.3(d). From a detailed perspective, there are clearly encapsulated cluster materials around the lithium dendrites, providing direct microscopic evidence for the source of the compressive stress identified in our operando strain data.

The physical mechanism underlying this transition from a 'kinetics-limited' to a 'stress-dominated' lithium plating regime can be elucidated through electro-chemo-mechanical coupling. At the onset of cryogenic charging, sluggish $\mathrm{Li^+}$ diffusion kinetics dictate the initial lithium deposition on the graphite surface. However, as plating proceeds, the newly deposited metallic lithium continuously reacts with the electrolyte, initiating a relentless 'fracture-repair-encapsulation' cycle of the SEI. At extremely low temperatures (e.g., around or below -20 °C), the newly formed SEI layer and accumulated 'dead lithium' composite become physically rigid. This dense, inflexible overlayer acts as a formidable mechanical constraint. Consequently, as further lithium plating attempts to proceed, it faces severe spatial confinement. The driving force for subsequent plating must overcome not only the electrochemical overpotential but also the immense mechanical compressive stress exerted by this rigid encapsulation layer. This macroscopically manifests as the continuous decay and anomalous suppression in the differential strain (dε/dQ), as the inward compressive stress counteracts the outward expansion of the electrode. Therefore, the plating behavior is flected by the mechanical yield strength of the SEI/dead-Li composite, marking the transition to a stress-dominated regime.

At the end of low-temperature charging, the differential strain changes from rising to falling, and this characteristic compression signal is directly derived from the encapsulation and densification of "dead lithium" by the growing solid electrolyte interface interphase. As shown in Fig. 3(f), the contractility of SEI exerts a significant inward compressive stress on the sediment, marking the transition of the lithium plating process from a dynamic stage limited by transport to a stress controlled stage dominated by interface mechanics reconstruction. In summary, our integrated analysis demonstrates a fundamental mechanistic transition in lithium plating below transitional temperature range (around –20 °C). The process evolves from a kinetics-limited regime, where ion diffusion controls deposition, to a stress-dominated regime, where the mechanical yield strength of the SEI/dead-Li composite become the primary constraint, dictating deposition morphology, triggering unique electrochemical signatures, and driving a distinct interfacial degradation pathway. This discovery recontextualizes ultra-low-temperature battery failure as a coupled electro-chemo-mechanical instability.

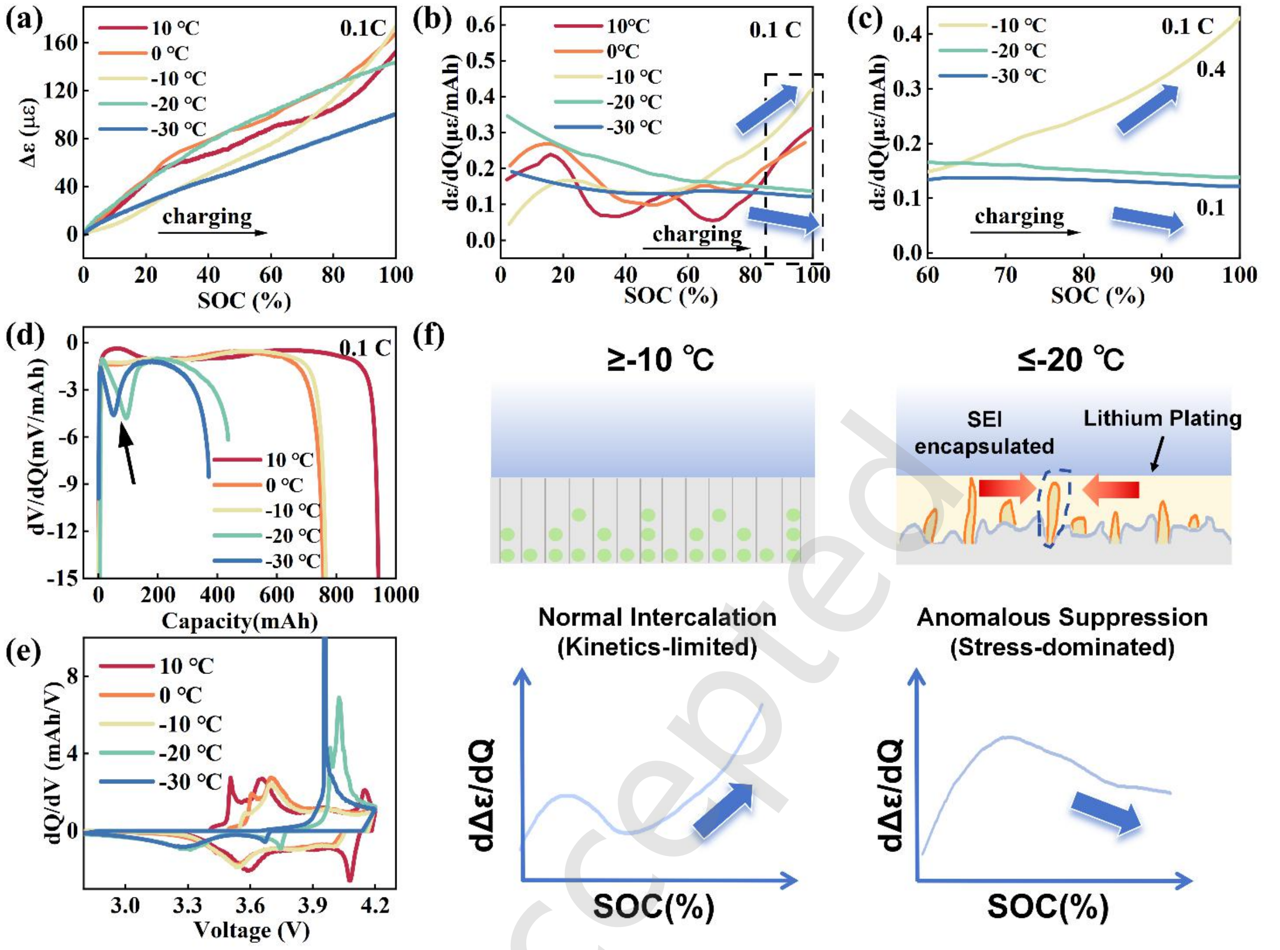

Figure 3 (a) Strain variation curve during 0.1C charging process at -30 ℃ to 10 ℃ (b) Strain differential curve diagram(dε/dQ) for 0.1C charging process at -30 ℃ to 10 ℃ (c) Enlarged view of the dε/dQ curves in the high SOC region (60%–100%) highlighting the quantitative divergence between normal intercalation and anomalous suppression. (d) dV/dQ for 0.1C discharging process at -30 ℃ to 10 ℃(e) dQ/dV diagram for 0.1C CC charging and discharging at -30 ℃ to 10 ℃ (f) Schematic diagram of the principle of capacity differential curve descent.

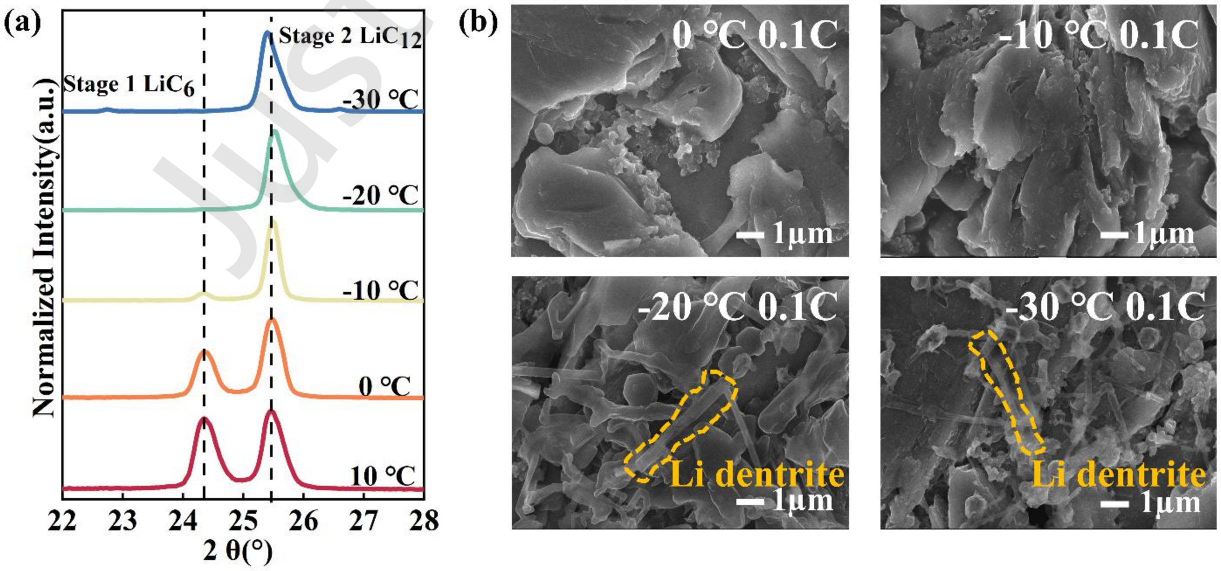

Figure 4 (a) XRD spectra of 0.1C charged anode electrode at -30 ℃ to 10 ℃ (b) SEM of 0.1C charged anode electrode at -30 ℃ to 0 ℃

2.3 Dynamic Competition and Long-Term Degradation

In order to further deepen the research, NCM||Gr batteries were cycled at 0.1C and low temperatures (-10 ℃, -20 ℃, -30 ℃) to induce lithium plating, with synchronous voltage monitoring. From the strain variation curve in Fig. 5(a-c) we can see that at -10 ℃ except for the first cycle, the changes in the strain curve are basically the same every cycle. At -20 ℃ and -30 ℃, the strain differential curve shows a flat state during the first few cycles of charging, corresponding to the lithium plating evolution in Fig.5(i). Critically, the curves at -20 °C and -30 °C roughly went through two stages. In the first stage, the absolute value of strain during the discharge process was greater than that during the charging process, that is, the strain baseline decreased. Then, the strain baseline increased, and the strain amplitude rapidly decreased and converged with the decrease of capacity. We plot their irreversible capacity accumulation values, i.e. the difference between charging capacity and discharging capacity, as a function of the number of cycles and the strain baseline value, i.e. the minimum value of the strain curve at each cycle, in the Fig. 5(d-f). It shows that compared with -10 °C, the first few cycles at -20 °C and -30 °C experienced a rapid increase in irreversible capacity accumulation and a decrease in strain baseline. The battery capacity and Coulomb efficiency have also undergone a similar process, with Coulomb efficiency rebounding after a previous decline as shown in Fig 5(g-h). By analyzing the dV/dQ lithium stripping peak during the discharge process in Fig.S6 in the ESM [33], it was found that the reversible lithium stripping amount experienced a decrease in the first few cycles at -20 °C, while it experienced a slight rebound at -30 °C.

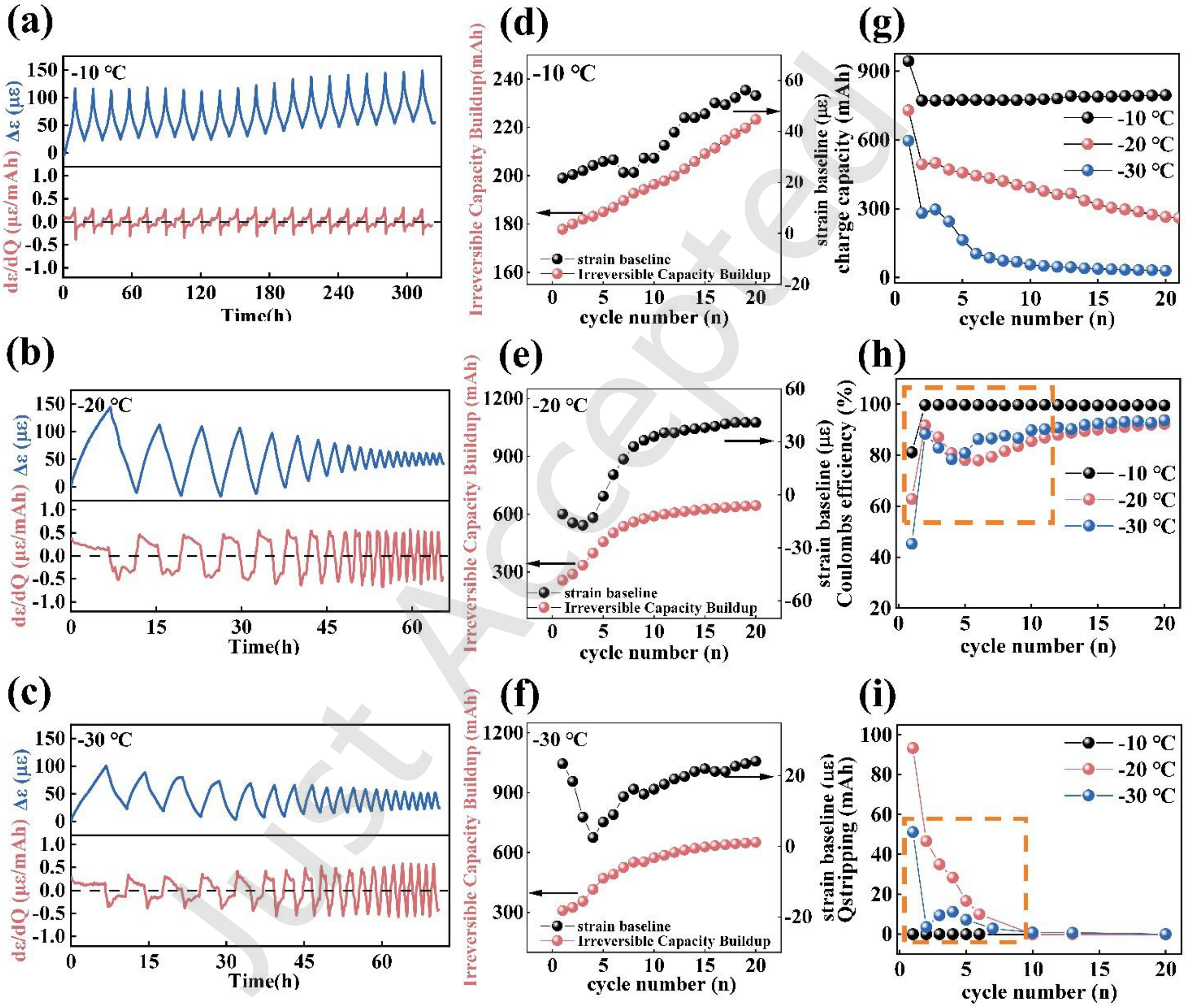

Figure 5 (a-c) Strain and differential strain variation charts for 0.1C at -10 °C, -20 °C and -30°C (d-f) Strain baseline and irreversible capacity buildup for 0.1C -10 °C, -20 °C and -30 °C (g)Charge capcacity for 20 cycles at -10°C, -20 °C and -30 °C (h) Coulombs efficiency for 0.1C at -10 °C, -20 °C and -30 °C (i) $Q_{\text{stripping}}$ extracted from dV/dQ for -10 °C, -20 °C and -30 °C.

Focusing on the extreme condition of -30 °C, we can see the complete evolution path from dynamic competition in early cycles to stress dominated failure after long-term cycles by coupling in-situ strain monitoring and multi-scale non in situ characterization. Multi-scale ex situ characterizations were conducted to corroborate these findings. The electrochemical onset is marked by an abnormally high peak in the dQ/dV curve during the first cycle in Fig. S7 in the Electronic Supplementary Material, signaling the initiation of massive lithium plating. In the subsequent early- stage (2nd–4th cycle), a distinct mechanical signature emerges: the absolute decrease in strain during discharge consistently exceeds the increase during charge within the same cycle. This asymmetry points to an interfacial- driven competition, attributed to an additional contraction component from the intense “reaction- encapsulation” process during discharge. Plan- sectional SEM in Fig. 7(a) directly visualizes lithium dendrites/agglomerates with significantly increased SEI encapsulation after discharge. As shown in Fig. 6(a), delithiation- induced contraction fractures the brittle SEI, exposing reactive lithium metal which undergoes vigorous side reactions and is rapidly encapsulated by new SEI, causing local densification and radial compression on the embedded FBG sensor.

This early- stage dynamic competition is corroborated by a multi- scale evidence chain. Cross-sectional diagram SEM in Fig. 7(a) reveals the corresponding electrode thickness evolution: an initial slight thinning after 1st cycle, consistent with local densification, followed by progressive thickening in 2nd to 4th cycle due to deposit accumulation and it reveals a distinct morphological evolution: the electrode laminate exhibits a significantly pulverized structure at 2nd and 4th cycle, which then transitions to a surprisingly smoothed and consolidated appearance by the 20th cycle. Plan-sectional SEM images in Fig. 7(a) at 1st, 2nd, 4th, and 20th cycle reveal that the graphite particles become increasingly fragmented, with a growing amount of by-products accumulated between the particles.

Structurally, in Fig. S8 in the Electronic Supplementary Material, the non- monotonic shift of the graphite (002) peak—moving to a lower angle from 1st cycle to 2nd cycle, then to a higher angle by the 4th cycle, and finally returning to a lower angle at the 20th cycle—provides a direct structural record of the evolving internal stress state. This sequence reflects a clear transition in the dominant source of mechanical stress: in the early stage, stress originated from the local mechanical effects of electrodeposition (plating); in the intermediate stage, stress evolved to be dominated by interfacial side- reactions and consumption; ultimately, stress became frozen by the macroscopic mechanical distortion caused by cumulative damage. Chemically, XPS analysis delineates a clear, stage- dependent evolution of the interfacial composition as shown in Fig. 7(b) and Figure S9 in the ESM. In the O 1s spectrum, the peak at 531 eV corresponds to C–O–Li, the peak at 532 eV corresponds to Li_2CO_3, and the peak at 533 eV corresponds to C–O. In the F 1s spectrum, the peak at 684.3 eV corresponds to LiF, the peak around 687 eV corresponds to $LiPF_6$, and the peak around 688 eV corresponds to PF_5. In the C 1s spectrum, the peak at 284.8 eV corresponds to C–C/C–H, the peak at 286 eV corresponds to C–O–C, and the peak at 288.5 eV corresponds to O–C=O. In the O1s spectra, the signal from lithium carbonate (Li_2CO_3) decreases from 56% at the 1st cycle to 32% at the 4th cycle and further to 20% by the 20th cycle, while that from C–O–Li species increases concurrently from 19% to 33% to 73% over the same period. By the 20th cycle, Li_2CO_3 is largely depleted and organic- polymeric C–O–Li becomes the dominant component. Conversely, the F1s spectra reveal a distinct trajectory, with lithium fluoride (LiF) decreasing from 34% at the 1st cycle to 30% at the 20th cycle. Crucially, the signal from PF_5- related species (from $LiPF_6$ decomposition) in the F1s spectra, while nearly absent at 2nd cycle and 4th cycle, re- emerges strongly by the 20th cycle to a level comparable to that at the 1st cycle. This chemical evolution provides direct molecular- level validation for the proposed mechanistic transition. The gradual shifts during the 2nd cycle to 4th cycle—the decrease in Li_2CO_3 from 56% to 32% and the increase in C–O–Li from 19% to 33%—mirror the period of intense interfacial activity and dynamic SEI repair. The dramatic reconfiguration by the 20th cycle—marked by the near- disappearance of solvent- derived Li_2CO_3, the dominance of polymer- like C–O- Li, and the reappearance of PF_5^- related species—signals the formation of a thick, stable, and inorganic- rich "dead" interphase. This chemically reconstituted interface is a direct consequence of sustained, stress- accelerated electrolyte decomposition in the stress- dominated regime. It is noteworthy that the mechanical signal of "discharge strain greater than charge strain" indicating the dynamic competition active period of the interface shows significant temporal differences between -20 °C and -30 °C, which profoundly reveals the regulatory effect of temperature on the evolution dynamics of failure paths. At -20 °C, the signal appeared from the first week and lasted for about three cycles, indicating that the interface reconstruction activity was rapidly initiated and maintained; At -30 °C, the signal is delayed until the 2nd to 4th cycle, forming a brief active window. This difference is due to the dual regulation of temperature on the rate of key interface processes: at -20 °C, a certain reaction activity allows for the rapid establishment and operation of dynamic competition between SEI repair and lithium re precipitation; At -30 °C, extreme kinetic limitations initially suppressed this competition until the accumulated damage in the cycle led to a relative increase in interfacial reactivity before triggering it.

Building upon the established correlation where the plateau in the charging strain differential curve signifies lithium deposition and its late-stage decline indicates dendritic growth, we uncover a dynamic competition mechanism dominant during the initial cycles under low-temperature, low-rate conditions. This "SEI repair–re-plating" mechanism involves the continuous fracture and repair of the solid electrolyte interphase, which perpetually exposes fresh electroactive sites on the anode surface, thereby reinitiating localized lithium deposition. The consistent "discharge strain > charge strain" signature provides direct mechanical evidence for the proposed cyclical competition, aligning with reported concepts of continuous SEI evolution and repair [37,38]. This phenomenon is rooted in the SEI's known mechanical instability—its repetitive fracture and reformation drives interfacial stress generation and active lithium consumption [39]. Operando studies further indicate that SEI repair proceeds via a solution-mediated, heterogeneous pathway that is highly sensitive to kinetic constraints [37]. In our low-temperature, kinetically-limited regime, we propose that a key asymmetry emerges: stress release and interfacial rearrangement during delithiation (discharge) become markedly more pronounced than during lithiation. This asymmetry, exacerbated by electrode heterogeneity, is precisely captured by our FBG sensors. Consequently, the gradual upward drift of the strain baseline correlates with irreversible capacity loss, marking the net accumulation of “dead lithium” and a thickened SEI [39]. Therefore, our study establishes that lithium plating does not occur in isolation; rather, through the mechanical stress it imposes, it actively drives the SEI's dynamic instability. This coupled electro-chemo-mechanical interplay—not plating alone—governs the long-term aging trajectory.

We employed optical fiber sensors to monitor the internal strain of batteries under low-temperature, long-cycle conditions. The evolution of the strain baseline provides critical insights into interfacial degradation: its general upward trend correlates with the accumulation of irreversible products like dead lithium, while temporary recoveries observed at -20 °C and -30 °C are attributed to the densification of the anode solid electrolyte interphase (SEI). This reveals the complex, competing dynamics between irreversible damage and interfacial reorganization under kinetically-limited conditions. Critically, complementing the established view that lithium plating primarily causes electrode expansion, our in-situ strain monitoring revealed an additional, subsequent mechanical phase: a distinctive decrease in differential strain during the late charging phase. This compressive signature is attributed to the SEI densifying around and encapsulating dead lithium, a mechanistic insight not accessible from conventional expansion or voltage-based diagnostics alone. This observation represents the first direct mechanical evidence linking the evolution of “dead Lithium” to a specific in-operando stress signature, demonstrating how localized stress variation can diagnose and elucidate dynamic interfacial processes in lithium-ion batteries.

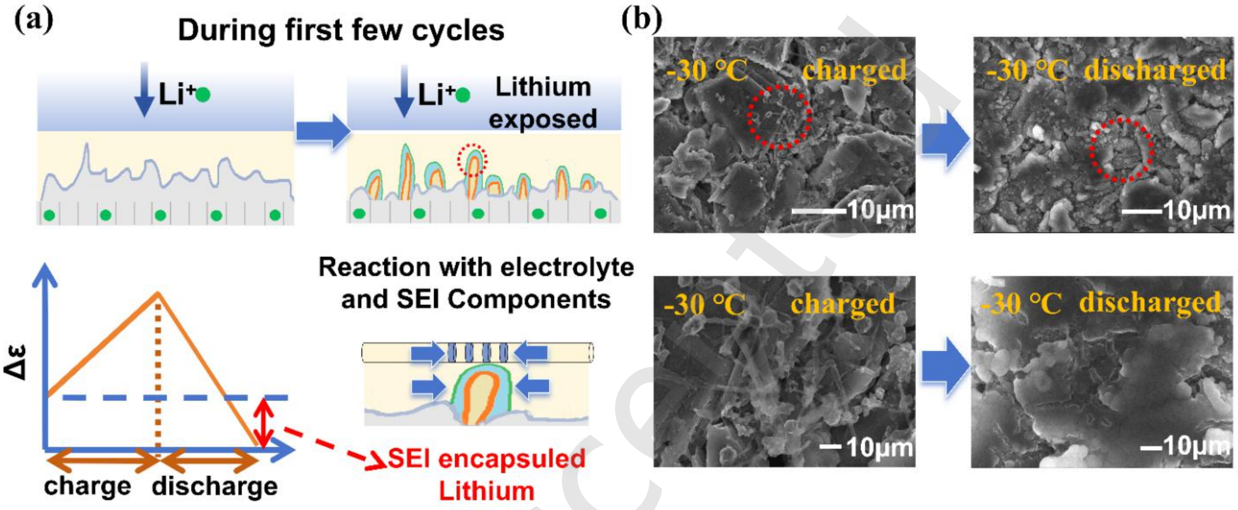

Figure 6 (a) Schematic diagram of the principle of the decreasing of strain baseline (b) Plan-sectional SEM of 0.1C charged and discharged anode electrode at -30 ℃.

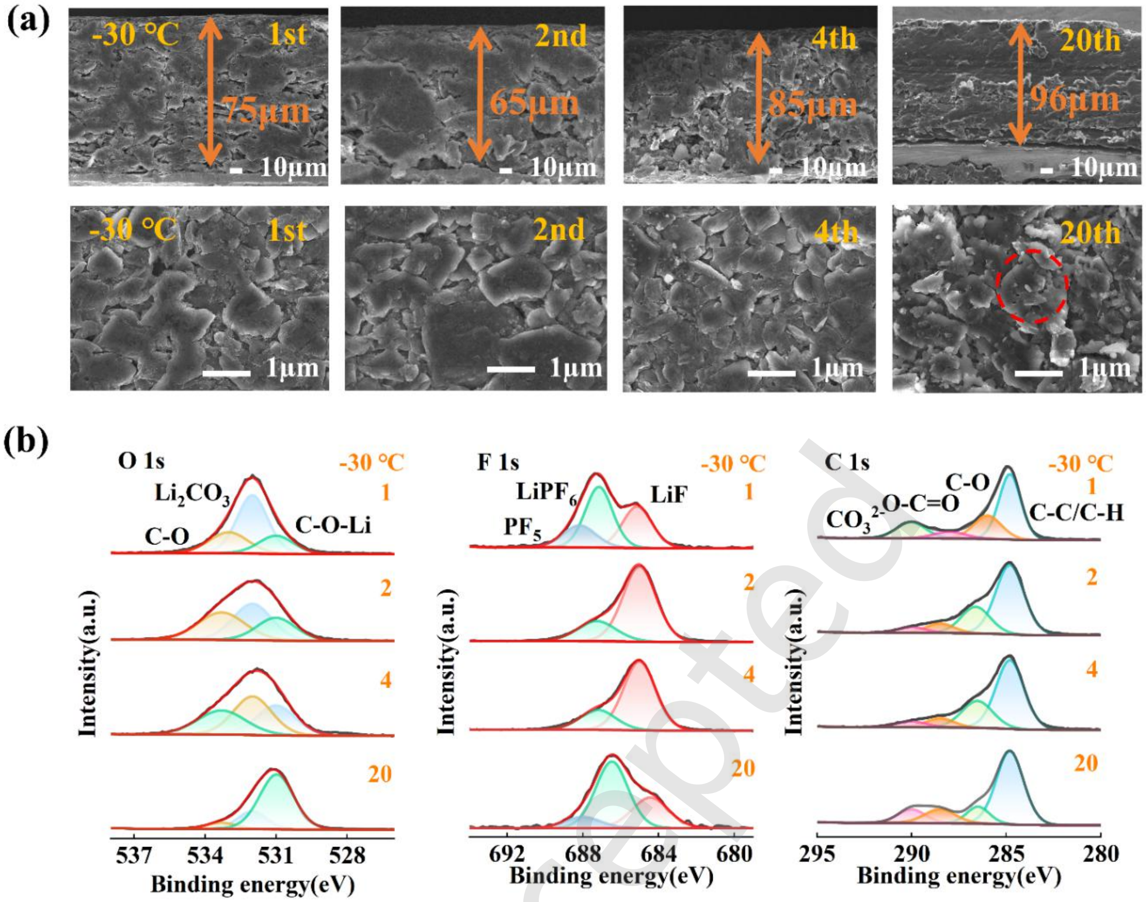

Figure 7 (a) Cross- sectional and Plan-sectional SEM of 0.1C discharged anode electrode at -30 ℃ for 1st,2nd,4th,20th cycle in cross-sectional view (b) X-ray photoelectron spectra of O1s, F1s and C1s of 0.1C discharged anode electrode at -30 ℃.

3 Conclusions

This study, through operando strain monitoring via embedded fiber Bragg grating (FBG) sensors combined with multi-scale electrochemical and physicochemical characterization, reveals a fundamental mechanistic transition in lithium plating behavior in lithium-ion batteries under cryogenic conditions. It was found that below a transitional temperature range (around −20 °C), the dominant mechanism of lithium plating shifts from kinetic limitation to stress domination. Under this stress-dominated regime, internal mechanical constraints generated by prior deposition become the core factor suppressing further electrode expansion and dictating interfacial evolution and the failure pathway. Direct mechanical evidence for this transition is the continuous decay and anomalous suppression in differential strain observed during the late charging phase at ultralow temperatures(e.g., a ∼50% quantitative decline at −30 °C). This macroscopic suppression physically originates from the immense compressive stress exerted by the continuously thickening and rigid SEI/dead-lithium encapsulation layer. This phenomenon is corroborated by a complete chain of evidence, including anomalous electrochemical signatures (abrupt switching in dQ/dV peaks), non-monotonic XRD peak shifts revealing compressive lattice distortion, and XPS compositional evolution indicative of intense interfacial reconstruction. Furthermore, the real-time strain signals, for the first time, captured and elucidated the dynamic "SEI repair-replating" competition during early low-temperature cycling, which macroscopically manifests as the unique feature of "discharge strain exceeding charge strain." This discovery directly links lithium plating to the mechanical instability of the SEI, clarifying their synergistic role in driving the long-term aging of batteries through a coupled mechanism. This work not only develops a highly sensitive mechanical sensing method for the in-situ diagnosis of battery failure but, more importantly, provides a novel perspective and theoretical foundation for understanding the electro-chemo-mechanical coupling that governs lithium plating under extreme operating conditions, offering critical guidance for designing safer battery systems.

Looking forward, future work should focus on multi-modal sensing integration, such as combining FBG with acoustic emission or ultrasonic detection, to achieve cross-validated, multi-parameter diagnostics. Extending this methodology to a broader range of temperatures, C-rates, and aging states will be essential for building robust failure maps. Specifically, considering the 10 °C temperature resolution in the current study, future investigations with finer temperature intervals (e.g., every 2 °C) are warranted to map out the exact boundary of this mechanistic transition. Ultimately, the strain signatures uncovered here pave the way for developing real-time, mechanical-signature-based early warning algorithms for battery management systems, potentially preventing hazardous plating before irreversible damage occurs.

4.Experimental set up

4.1 Principle of FBG

FBG sensors play a vital role in diverse applications ranging from structural health monitoring to healthcare, showcasing their versatility and potential for future advancements. Here we talk about traditional FBG sensors in the general application scenarios. FBG sensors are optical devices fabricated by periodically modulating the refractive index of a section of optical fiber. With high level of sensitivity, FBG functions as highly selective wavelength-selective reflectors, enabling precise measurements of physical parameters such as temperature and strain. The sensing mechanism is based on the Bragg condition, where light of a specific wavelength is reflected back along the fiber when it encounters the periodic variation in refractive index. Changes in temperature or strain alter the refractive index and grating period of the fiber, leading to a shift in the Bragg wavelength (λ_B). This wavelength shift is proportional to the change in the measured parameter, allowing for accurate and high-resolution sensing. The specific formula is as followed:

$$\lambda_B = 2\Lambda n_{eff} \quad (1)$$

In the formula: Λ is the grating period; n_{eff} is the effective refractive index of the fiber core; λ_B is the Bragg wavelength. The grating structure reflects a specific wavelength λ_B and transmits the remaining wavelengths of optical signals. The Bragg wavelength is closely related to the refractive index of the fiber and the grating period, therefore, the Bragg wavelength is a powerful indicator of changes in external environmental parameters of the fiber. In FBG sensors, when temperature causes thermal expansion of the fiber and changes in the refractive index of the fiber, the shift in Bragg wavelength caused by temperature changes can be expressed as [41,42]

$$\Delta\lambda_B/\lambda_B=(\alpha+\xi)\Delta T \quad (2)$$

In the formula: ΔT is the temperature change at the FBG sensor; α represents the coefficient of thermal expansion; ξ represents the thermal optical coefficient. When the battery changes in temperature or strain, the spacing between FBG grids changes, and the center wavelength of reflected light changes. The displacement of the central wavelength is linearly related to temperature and strain. In addition, other physical parameters such as pressure and vibration and other condition that can influence Λ and neff. Likewise, when there is strain shift,

$$\Delta\lambda_B/\lambda_B=(1-p_e)\Delta\varepsilon \quad (3)$$

Where p_e presents the effective photo-elastic coefficient. Hence undermining micro changes of other condition,

$$\Delta\lambda_B = K_\varepsilon\cdot\Delta\varepsilon + K_T\,\Delta T \quad (4)$$

Because of the principle mentioned above, there is a linear relation between temperature or strain with the wavelength shift. Under the help of optical interrogator, ΔT and $\Delta\varepsilon$ can be easily detected. Normally, the diameter of an optical fiber is 0.25μm with a PVC protection tube attached to the external surface of a bare fiber. When embedded and buried in materials consist of Particles and binders such as PVDF, it bears stress from all directions, so a comprehension reflection of strain is obtained. With hook's law:

$$\sigma=E\cdot\varepsilon \quad (5)$$

as long as we get the elastic modulus of the fiber (normally 78 GPa), the stress that the fiber withstand can be calculated.

4.2 Fiber Bragg Grating Sensors

The FBG sensors were inscribed on commercially available photosensitive optical fiber purchased from (Wuhan HEXAPHASE OPTOELECTRONIC TECHNOLOGY CO., LTD) by the phase mask method. The UV radiation system used was a pulsedexcimer laser (KrF), emitting at an range of wavelength of 1538-1558 nm. The Bragg wavelength variations were monitored using an interrogation system (HEXA-DEM-1000) with a sample rate of 100 Hz and a wavelength accuracy of 1 pm.

4.3 Li-Ion Cell Assembly and Microsensor Integration

The commercial-grade Li-ion pouch cells were customized and purchased from Li-FUN Technology Corporation Limited. The cathode is composed of NCM811 (active mass loading: 14 mg cm^{-2}), and the anode is artificial graphite (active mass loading: 9.9 mg cm^{-2}). The cell assembly and sensor integration were conducted inside a highly controlled dry room (dew point: –30 °C), where all materials were stored prior to use. The electrolyte was provided by DoDo Chem.

To achieve operando internal strain monitoring, the FBG microsensor (bare silica fiber, 125 μm in diameter) was carefully embedded directly at the center of the electrode/separator interface, with both ends securely fixed using tab films. During operation, the top and bottom surfaces of the pouch cell were constrained by rigid fixtures. This geometric confinement forces the internal volume expansion (swelling) generated during charging and discharging to manifest entirely as measurable, highly sensitive longitudinal strain along the FBG sensor. Unlike previously reported external pressure sensors [26] that only capture macroscopic casing deformation, this internal FBG configuration enables high-resolution monitoring of local electro-chemo-mechanical strain variations at the electrode sheet level without interference from the cell packaging.

To ensure the absolute reliability of this internal sensing approach, the integration impact, sensor stability, and potential thermal artifacts were systematically evaluated. The fused silica (SiO_2) core of the FBG, coated with a thin polyimide (PI) protective layer, is highly electrochemically inert and mechanically robust within the battery's operational voltage window, ensuring long-term signal stability. The micro-scale integration introducing negligible disturbance to the cell's electrochemical performance was confirmed by long-term cycling tests, as shown in Figure S10 (Electronic Supplementary Material).

Furthermore, regarding the intrinsic temperature-strain coupling of FBG sensors $\Delta\lambda_B = K_\varepsilon\cdot\Delta\varepsilon + K_T\,\Delta T$, the thermal artifact was quantitatively decoupled to isolate the true mechanical strain. The calibrated strain and temperature sensitivities of the deployed FBG are ~1.2 pm/με and ~10 pm/°C, respectively. Because the batteries were cycled at a very low C-rate (0.1 C) inside a high-precision isothermal environmental chamber with active thermal regulation, the maximum Joule heating and surface temperature fluctuation (ΔT) were maintained well within 1.4 °C. This excellent thermal stability was experimentally verified by a

~28-hour long-term monitoring test at −30 °C, showing peak-to-peak fluctuations consistently within 1.4 °C (Figure S11 in Electronic Supplementary Material). This minimal thermal fluctuation translates to a maximum wavelength shift of ~14 pm, equivalent to an apparent strain artifact of merely ~11.7 με. Given that the operational chemo-mechanical strain reached up to ~160 με, the thermal interference accounts for only a marginal ~7.3% of the total signal magnitude. Moreover, the monotonic and gradual nature of any slight temperature rise mathematically cannot induce the profound, continuous decay observed in the differential strain (dε/dQ) signatures. Thus, the real-time FBG signals predominantly and accurately reflect the internal electro-chemo-mechanical strain evolution.

4.4 Electrochemical Testing

Before the experiment, the pressure was set at 17N (~3.5 kPa) for a duration of 4 hours to ensure no further strain fluctuations occurred before the charge-discharge cycle began. The fixture device used in previous literature effectively applies appropriate pressure to the battery [43]. The optical fiber is mounted on the electrode plate, with both ends secured by tab adhesive. Due to the significant applied pressure, the grating can be precisely positioned at the center of the battery cycling tests were performed using a charge and discharge tester (Wuhan LAND Electronic Co. Ltd) at different C rates. During battery testing, the battery was placed in a low-temperature chamber, and the temperature was maintained well. The low-temperature chamber was purchased from SDAKA Company. Three batteries underwent constant-current (CC) tests at 10 °C, 0 °C, and-10 °C, with current rates of 0.1C, 0.2C, 0.3C, 0.4C, and 0.5C respectively. Each rate cycle was conducted for two cycles, followed by a 10-minute rest period. During the long-cycle test, all four batteries were tested at-40 °C, -30 °C, and-10 °C. The charging rate of the battery operating at-40 °C is 0.02 C, while the others are 0.1C.

Electronic Supplementary Material: Supplementary material (please provide the brief detail of the ESM) is available in the online version of this article at https://doi.org/10.26599/NR.2026.94908758.

Data availability

All data needed to support the conclusions in the paper are presented in the manuscript and the Electronic Supplementary Material. Additional data related to this paper may be requested from the corresponding author upon request.

Acknowledgements

None

Declaration of competing interest

All the contributing authors report no conflict of interests in this work.

Author contribution statement

Fan Zhang: Data curation, project administration, validation, writing manuscript, experimental design.
Di Lu: Data curation, project administration, validation, experimental design.
Xianxian Shi: Project administration.
Shu Hong: Project administration.
Peitao Xiao: Project administration, funding acquisition.
Yufang Chen: Project administration, funding acquisition, writing manuscript.
All the authors have approved the final manuscript."

Informed consent

Not applicable

Ethics statement

Not applicable

Use of AI statement

During the preparation of this work, the authors used Grammarly in order to language polishing. After using this tool/service, the authors reviewed and edited the content as needed and take full responsibility for the content of the publication.

References

[1] Ahlgren, P.; Jeppsson, T.; Stenberg, E.; Berg, E.; Edström, K. BATTERY 2030^+ and its Research Roadmap: A Bibliometric Analysis. *ChemSusChem* **2023**, *16*, e202300333.

[2] Dong, Y.; Liu, C.; Rui, M.; Zhang, X.; Guan, Y.; Chen, L.; Huang, Q.; Wang, M.; Su, Y.; Wu, F.; Li, N. Review on Graphite Anodes for Fast-Charging Lithium-Ion Batteries: Mechanism, Modification and Characterizations. *Adv. Funct. Mater.* **2025**, *35*, 2506190.

[3] Zhao, X.; Yin, Y.; Hu, Y.; Choe, S.-Y. Electrochemical-thermal modeling of lithium plating/stripping of $Li(Ni_{0.6}Mn_{0.2}Co_{0.2})O_2$/Carbon lithium-ion batteries at subzero ambient temperatures. *J. Power Sources* **2019**, *418*, 61–73.

[4] Waldmann, T.; Hogg, B.-I.; Kasper, M.; Grolleau, S.; Couceiro, C. G.; Trad, K.; Matadi, B. P.; Wohlfahrt-Mehrens, M. Interplay of Operational Parameters on Lithium Deposition in Lithium-Ion Cells: Systematic Measurements with Reconstructed 3-Electrode Pouch Full Cells. *J. Electrochem. Soc.* **2016**, *163*, A1232–A1238.

[5] Zhao, Y.; Spingler, F. B.; Patel, Y.; Offer, G. J.; Jossen, A. Localized Swelling Inhomogeneity Detection in Lithium Ion Cells Using Multi-Dimensional Laser Scanning. *J. Electrochem. Soc.* **2019**, *166*, A2742–A2751.

[6] Günter, F. J.; Burgstaller, C.; Konwitschny, F.; Reinhart, G. Influence of the Electrolyte Quantity on Lithium-Ion Cells. *J. Electrochem. Soc.* **2019**, *166*, A1709–A1714.

[7] Zhao, D.; Ding, M.; Tao, M.; Shan, P.; Lin, H.; Chen, Y.; Chen, J.; Zhou, Y.; Yang, Y. Advanced Interfacial Engineering of Graphite Anodes for Next-Generation Lithium-Ion Batteries. *Small* **2025**, *21*, e12150.

[8] Tian, Y.; Lin, C.; Li, H.; Du, J.; Xiong, R. Detecting undesired lithium plating on anodes for lithium-ion batteries – A review on the in-situ methods. *Appl. Energy* **2021**, *300*, 117386.

[9] Wu, E. A.; Kompella, C. S.; Zhu, Z.; Lee, J. Z.; Lee, S. C.; Chu, I.-H.; Nguyen, H.; Ong, S. P.; Banerjee, A.; Meng, Y. S. New insights into the interphase between the Na metal anode and sulfide solid-state electrolytes: a joint experimental and computational study. *ACS Appl. Mater. Interfaces* **2018**, *10*, 10076–10086.

[10] Yan, C.; Zhang, Q. Towards the Intercalation and Lithium Plating Mechanism for High Safety and Fast-Charging Lithium-ion Batteries: A Review. *Energy Lab* **2022**, *1*, 20220011.

[11] Campbell, I. D.; Marzook, M.; Marinescu, M.; Offer, G. J. How Observable Is Lithium Plating? Differential Voltage Analysis to Identify and Quantify Lithium Plating Following Fast Charging of Cold Lithium-Ion Batteries. *J. Electrochem. Soc.* **2019**, *166*, A725–A739.

[12] Tanim, T. R.; Dufek, E. J.; Dickerson, C. C.; Wood, S. M. Electrochemical Quantification of Lithium Plating: Challenges and Considerations. *J. Electrochem. Soc.* **2019**, *166*, A2689–A2696.

[13] Sieg, J.; Storch, M.; Fath, J.; Nuhic, A.; Bandlow, J.; Spier, B.; Sauer, D.

U. Local degradation and differential voltage analysis of aged lithium-ion pouch cells. *J. Energy Storage* **2020**, *30*, 101582.

[14] Wang, S.; Ren, D.; Xu, C.; Han, X.; Liu, X.; Lu, L.; Ouyang, M. Lithium plating induced volume expansion overshoot of lithium-ion batteries: Experimental analysis and modeling. *J. Power Sources* **2024**, *593*, 233946.

[15] Zhu, J.; Dewi Darma, M. S.; Knapp, M.; Sørensen, D. R.; Heere, M.; Fang, Q.; Wang, X.; Dai, H.; Mereacre, L.; Senyshyn, A.; Wei, X.; Ehrenberg, H. Investigation of lithium-ion battery degradation mechanisms by combining differential voltage analysis and alternating current impedance. *J. Power Sources* **2020**, *448*, 227575.

[16] Dubarry, M.; Svoboda, V.; Hwu, R.; Liaw, B. Y. Incremental Capacity Analysis and Close-to-Equilibrium OCV Measurements to Quantify Capacity Fade in Commercial Rechargeable Lithium Batteries. *Electrochem. Solid-State Lett.* **2006**, *9*, A454–A457.

[17] Ringbeck, F.; Rahe, C.; Fuchs, G.; Sauer, D. U. Identification of Lithium Plating in Lithium-Ion Batteries by Electrical and Optical Methods. *J. Electrochem. Soc.* **2020**, *167*, 090536.

[18] Yang, X.-G.; Ge, S.; Liu, T.; Leng, Y.; Wang, C.-Y. A look into the voltage plateau signal for detection and quantification of lithium plating in lithium-ion cells. *J. Power Sources* **2018**, *395*, 251–261.

[19] Anseán, D.; Dubarry, M.; Devie, A.; Liaw, B. Y.; García, V. M.; Viera, J. C.; González, M. Operando lithium plating quantification and early detection of a commercial $LiFePO_4$ cell cycled under dynamic driving schedule. *J. Power Sources* **2017**, *356*, 36–46.

[20] Li, J.; Wang, L.; Xu, J. Investigation of the lithium plating triggering criterion in graphite electrodes. *J. Mater. Chem. A* **2024**, 12, 12581–12591.

[21] Petzl, M.; Danzer, M. A. Nondestructive detection, characterization, and quantification of lithium plating in commercial lithium-ion batteries. *J. Power Sources* **2014**, *254*, 80–87.

[22] Adam, A.; Knobbe, E.; Wandt, J.; Kwade, A. Application of the differential charging voltage analysis to determine the onset of lithium-plating during fast charging of lithium-ion cells. *J. Power Sources* **2021**, *495*, 229794.

[23] Kirchner-Burles, C.; Fordham, A.; Reid, H. T.; Johnson, M.; Buckwell, M.; Iacoviello, F.; Coke, K.; Jervis, R.; Hinds, G.; Shearing, P. R.; Robinson, J. B. Safety and performance implications of lithium plating induced by sub-zero temperature cycling of lithium-ion batteries. *J. Power Sources* **2025**, *660*, 238565.

[24] Liu, B.; Liu, X.; Wang, H.; Li, J.; Xu, J. A Hierarchical Modeling Framework for Electrochemical Behaviors in Lithium‐Ion Batteries with Detailed Structures. *Energy Environ. Mater.* **2024**, 7, e12711.

[25] Chang, C.; Li, X.; Sun, Y.; Jiang, J.; Tian, A.; Lv, L.; Gao, Y. Force-signal driven real-time lithium plating detection in mechanically constrained $LiFePO_4$ pouch cells. *Energy* **2025**, *323*, 135780.

[26] Huang, W.; Ye, Y.; Chen, H.; Vila, R. A.; Xiang, A.; Wang, H.; Chen, F.; Liu, Y.; Wang, L.; Li, Y.; Cui, Y. Onboard early detection and mitigation of lithium plating in fast-charging batteries. *Nat. Commun*. **2022**, *13*, 7091.

[27] Peng, Y.; Ding, M.; Zhang, K.; Zhang, H.; Hu, Y.; Lin, Y.; Hu, W.; Liao, Y.; Tang, S.; Liang, J.; Wei, Y.; Gong, Z.; Jin, Y.; Yang, Y. Quantitative Analysis of the Coupled Mechanisms of Lithium Plating, SEI Growth, and Electrolyte Decomposition in Fast Charging Battery. *ACS Energy Lett.* **2024**, *9*, 6022–6028.

[28] Lin, H.; Hu, Y.; Zhou, Y.; Hu, W.; Lin, J.; Luo, H.; Jin, Y.; Zhao, D.; Chen, J.; Tao, M.; Shan, P.; Liang, J.; Wei, Y.; Yang, Y. Unveiling the Onset, Evolution, and Kinetic Factors Associated with Lithium Plating on Graphite Electrodes in Lithium-ion Batteries. *Adv. Energy Mater.* **2025**, *15*, e02728.

[29] Lin, Y.; Hu, W.; Ding, M.; Hu, Y.; Peng, Y.; Liang, J.; Wei, Y.; Fu, A.; Lin, J.; Yang, Y. Unveiling the Three Stages of Li Plating and Dynamic Evolution Processes in Pouch C/$LiFePO_4$ Batteries. *Adv. Energy Mater.* **2024**, *14*, 2400894.

[30] Zhu, Y.; Yan, L.; Han, S.; Gu, M.; Ma, S.; Luo, Y.; Meng, A.; Zhao, C.; Xie, J.; Yang, C.; Li, Q. In situ lithium plating monitor for lithium-ion batteries enabled by operando pressure detection. *J. Power Sources* **2025**, *631*, 236281.

[31] Chen, Z.; Zhang, C.; Cai, X.; Liu, M.; Qiao, B.; Zhang, L.; Jiang, J.; Yang, X.-G. Operando detection for lithium plating in lithium-ion batteries via expansion force signal decoupling. *J. Power Sources* **2026**, *661*, 238644.

[32] Bhowmick, A.; Rui, B.; Sun, S.; Tan, X.; Wei, B.; Hahn, Y.; Kulathu, S.; Oancea, V.; Lu, W.; Xu, J. Electrochemo-mechanics unlocks hidden dynamics of lithium plating under stacking pressure. *Nano Energy* **2026**, 150, 111751.

[33] Li, G.; Zhang, T.; Tang, J.; Liu, M.; Xie, Y.; Yu, J.; Hui, X.; Deng, C.; Lu, X.; Kim, Y.; Huang, J.; Xu, Z. Decoding Chemo-Mechanical Failure Mechanisms of Solid-State Lithium Metal Battery Under Low Stack Pressure via Optical Fiber Sensors. *Adv. Mater.* **2025**, *37*, e202417770.

[34] Yadegari, H.; Koronfel, M. A.; Wang, K.; Thornton, D. B.; Stephens, I. E. L.; Molteni, C.; Haynes, P. D.; Ryan, M. P. Operando Measurement of Layer Breathing Modes in Lithiated Graphite. *ACS Energy Lett.* **2021**, *6*, 1633–1638.

[35] Louli, A. J.; Ellis, L. D.; Dahn, J. R. Operando Pressure Measurements Reveal Solid Electrolyte Interphase Growth to Rank Li-Ion Cell Performance. *Joule* **2019**, *3*, 745–761.

[36] Mei, W.; Zhang, L.; Sun, J.; Wang, Q. Experimental and numerical methods to investigate the overcharge caused lithium plating for lithium ion battery. *Energy Storage Mater.* **2020**, *32*, 91–104.

[37] He, Y.; Wang, J.; Wang, L.; He, X. Thermodynamic Understanding of Formation and Evolution of Solid Electrolyte Interface in Li-Ion Batteries. *Batteries Supercaps* **2024**, *7*, e202400059.

[38] Heiskanen, S. K.; Kim, J.; Lucht, B. L. Generation and Evolution of the Solid Electrolyte Interphase of Lithium-Ion Batteries. *Joule* **2019**, *3*, 2322–2333.

[39] Qiao, D.; Wei, X.; Zhu, J.; Zhang, G.; Yang, S.; Wang, X.; Jiang, B.; Lai, X.; Zheng, Y.; Dai, H. Mechanism of battery expansion failure due to excess solid electrolyte interphase growth in lithium-ion batteries. *Nano Energy* **2025**, *128*, 110185.

[40] Wang, Y.; Leau, C.; Coudray, S.; Boussard-Plédel, C.; Davoisne, C.; Foix, D.; Gervillié-Mouravieff, C.; Boles, S. T.; Tarascon, J.-M. Formation dynamics of an ethylene carbonate-derived solid–electrolyte-interphase in commercial Li-ion batteries. *Energy Environ. Sci*. **2026**, *19*, 456–467.

[41] Campanella, C.; Cuccovillo, A.; Campanella, C.; Yurt, A.; Passaro, V. Fibre Bragg Grating Based Strain Sensors: Review of Technology and Applications. *Sensors* **2018**, *18*, 3115.

[42] Wu, Q.; Cheng, Y.; Huang, X.; Wei, Q.; Chen, J. Operando strain and temperature measurement of sodium-ion batteries via optical fiber sensors. *Opt. Commun.* **2025**, *577*, 131428.

[43] Liu, D.; Wu, B.; Xu, Y.; Ellis, J.; Baranovskiy, A.; Lu, D.; Lochala, J.; Anderson, C.; Baar, K.; Qu, D.; Yang, J.; Galvez-Aranda, D.; Lopez, K.-J.; Balbuena, P. B.; Seminario, J. M.; Liu, J.; Xiao, J. Controlled large-area lithium deposition to reduce swelling of high-energy lithium metal pouch cells in liquid electrolytes. *Nat. Energy* **2024**, *9*, 835–846.

Electronic Supplementary Material

Decoding lithium plating evolution at ultralow temperatures through real-time FBG strain monitoring

Fan Zhang[1], Di Lu[1], Peitao Xiao[1], Xianxian Shi[1], Shu Hong[2], and Yufang Chen[1].

[1] *College of Aerospace Science and Engineering, National University of Defense Technology, Changsha 410000, China*
[2] *Tianjin Lishen Battery Joint Stock Company Limited, No.6, Lanyuan Road, Huayuan Industrial Park, Tianjinn 300384, China*

Address correspondence to Di Lu, ludi@nudt.edu.cn; Yufang Chen, chenyufang@nudt.edu.cn

Supporting information to https://doi.org/10.26599/NR.2026.94908758

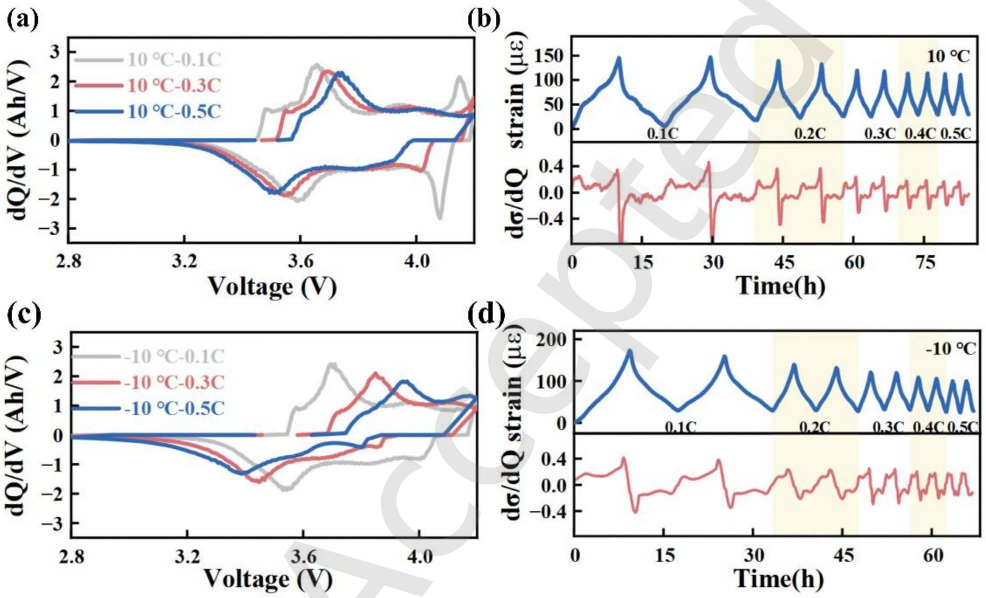

Figure S1 Strain and differential strain variation charts at 10°C**(a-b)**, -10°C**(c-d)**, as well as their dQ/dV charts at 0.1C, 0.3C, and 0.5C.

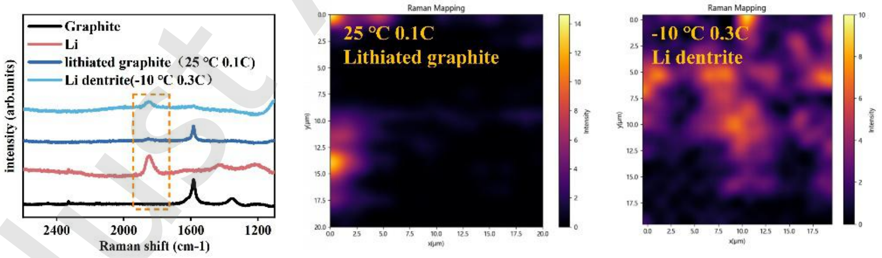

Figure S2 Raman surface scanning image of 0.1C charged anode electrode at -25 °C and of 0.3C charged anode electrode at -10 °C.

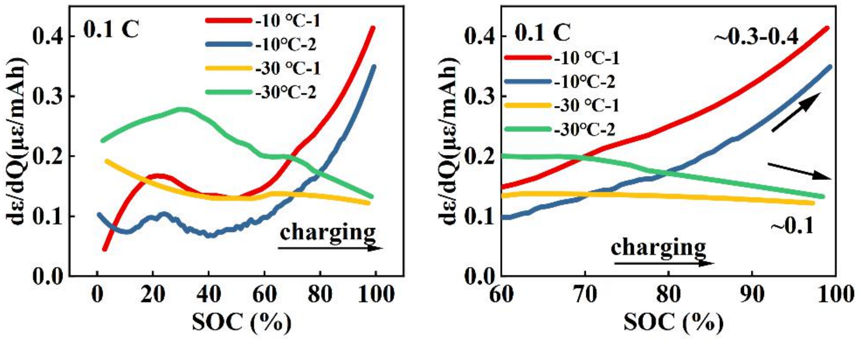

Figure S3. Reproducibility of differential strain ($d\varepsilon/dQ$) signatures across multiple parallel cells at the boundary temperatures .

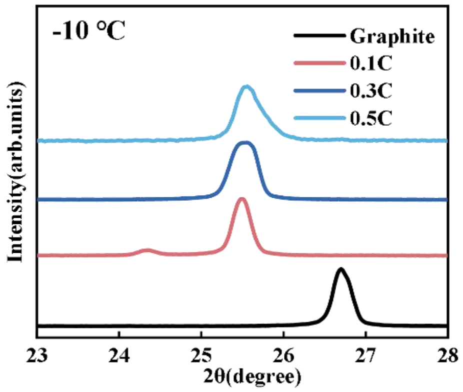

Figure S4 XRD spectra of Graphite, 0.1C,0.3C,0.5C charged graphite electrode at -10 °C.

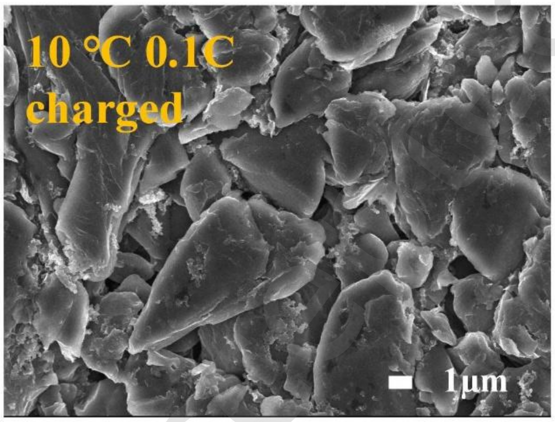

Figure S5 SEM images of the anode electrodes charged at 0.1C at 10°C.

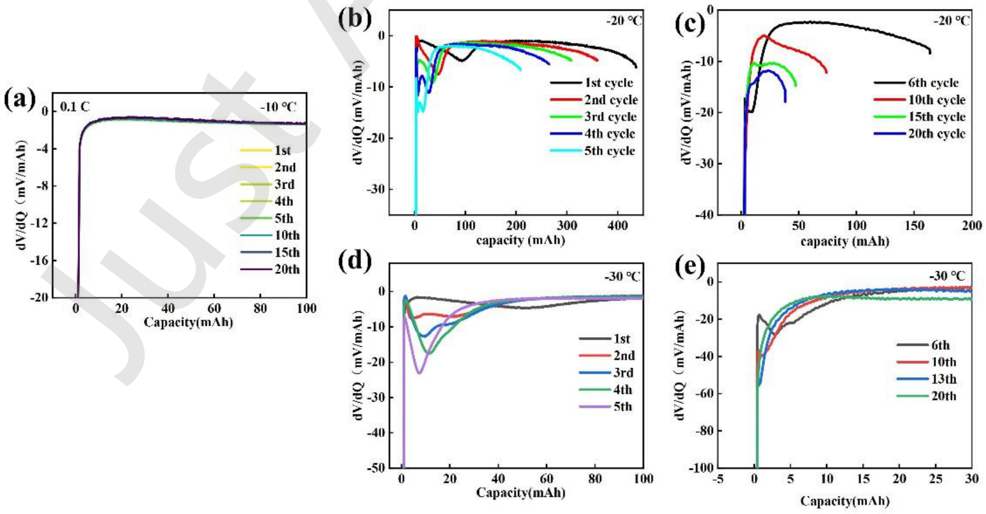

Figure S6 dV/dQ curve during discharging at -10 °C, -20 °C and -30 °C.

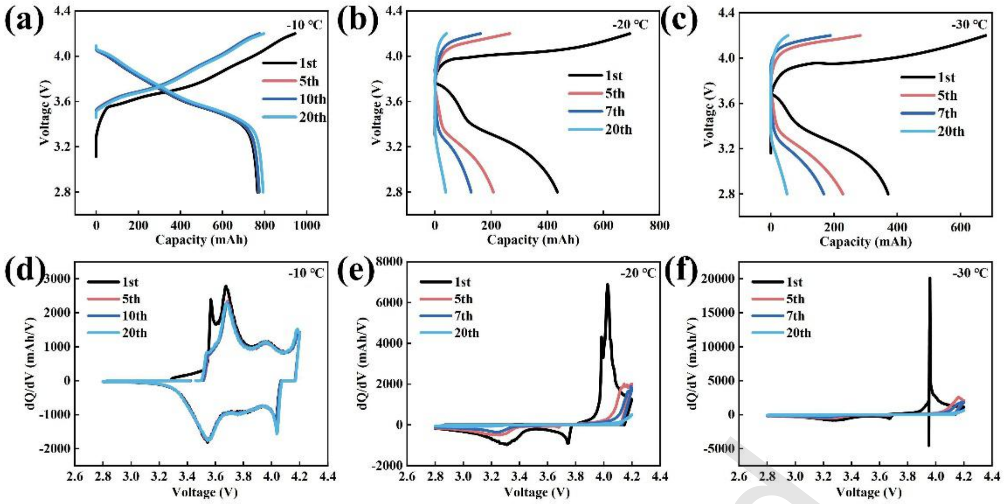

Figure S7 Voltage-capacity curve and dQ/dV curve at -10 °C(a,d), -20 °C(b,e) and -30 °C(c,f).

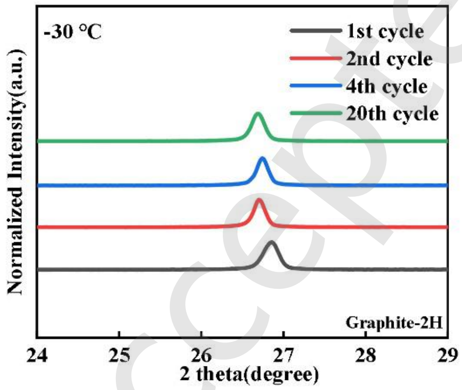

Figure S8 XRD spectra of anode electrode for 1st,2nd,4th and 20th cycle at -30 °C.

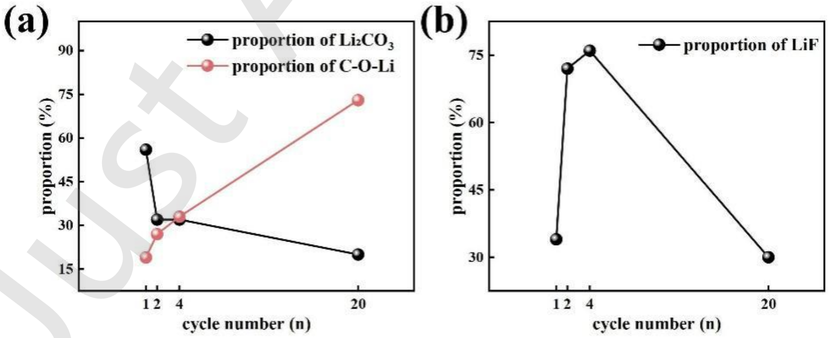

Figure S9 (a) Changes in the content of $Li_2CO_3$and C-O-Li in O1s at 1st, 2nd, 4th, and 20th cycle (b) Changes in the content of LiF in F1s at 1st, 2nd, 4th, and 20th cycle

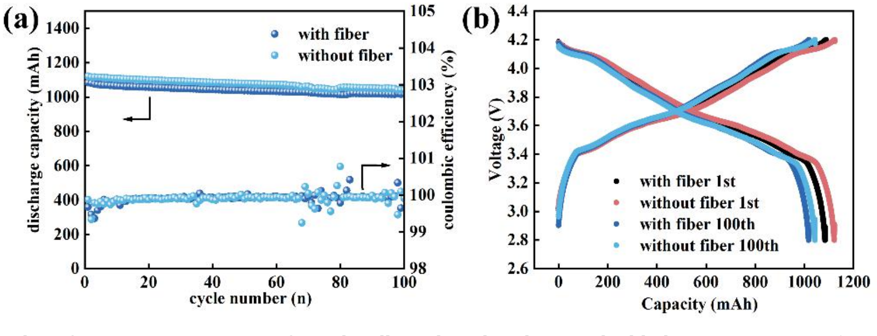

Figure S10. Electrochemical performance comparison of pouch cells with and without embedded FBG sensors at 25 °C (0.1 C cycling). (a) Discharge capacity and Coulombic efficiency over 100 cycles. (b) Charge-discharge voltage profiles at the 1st and 100th cycles. The results confirm that the integration of the FBG sensor has negligible impact on the cell's electrochemical performance.

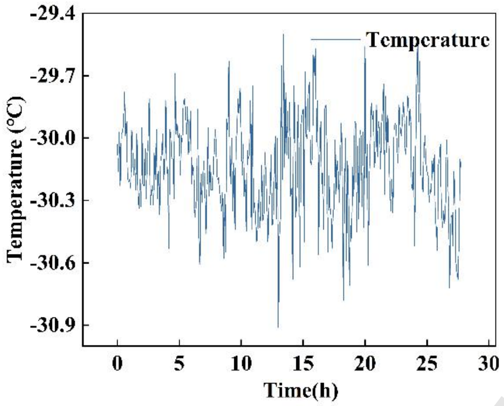

Figure S11 Long-term temperature stability test of the high-precision isothermal environmental chamber at a setpoint of –30 °C over a period of ~28 hours by thermocouple.